Supplemental Information for

Response to dynamic shape changes in suspensions of hard rectangles

Denis Dertli and Thomas Speck
Institute for Theoretical Physics IV, University of Stuttgart, Heisenbergstr. 3, 70569 Stuttgart, Germany

S1. SIMULATION PROTOCOL

We perform hard-particle Monte Carlo simulations in the NVT ensemble using `HOOMD-blue` [1–4] mixing local translation and rotation of particles with moves that attempt to transform the particle shape. For all runs, the maximum size of translation and rotation trial moves are fixed, and individual random number seeds are used. Our simulations proceed according to the protocol sketched in Fig. S1 consisting of five steps (valid for both the morphing and cascading shape transformation protocol):

R1: The protocol randomizes an initial lattice configuration (C1) for $\tau_{\mathrm{rdm}} \sim 10^6$ Monte Carlo time steps[1].

R2: We now expand the system and let the simulation run for $\tau_\phi < 10^7$ until the prescribed packing fraction ϕ is reached.

R3: We then perform a short pre-relaxation for $\tau_{\mathrm{pr}} \sim 10^6$ Monte Carlo time steps. At this point, the preparation of our system (C4) is accomplished.

R4: Now, we trigger the shape transformation, i.e., during one Monte Carlo time step $\Delta\tau_{\mathrm{d}}^* = 1$, all particles either attempt one local trial move[2] or a small shape update attempt of $\Delta\zeta = 10^{-6}$[3]. By construction, if a shape update attempt results in a configuration with overlaps, we reject it and perform another translation/rotation move. Thus, in general, $\zeta \not\sim \tau$. For consistency with the other runs (without shape transformations), we introduce the quantity τ_{d} that only counts the number of accepted local moves (translation or rotation but not shape updates), i.e., $\tau_{\mathrm{d}} < \tau_{\mathrm{d}}^*$. Accordingly, we stick to the overall definition that $\Delta\tau_{\mathrm{d}} = \Delta\tau = 1$ represents the order of magnitude of performed local (translation or rotation) trial moves per particle. This is also a reasonable choice in view of the fact that the shape updates have no (direct) effect on our collective variables (MSD or order parameters) and leave their values invariant, because neither position nor orientation is (directly) changed. In steps of $\Delta\tau_{\mathrm{d}} \sim 10^3$, we periodically collect configurations. The simulation is run until either the final shape is reached ($\zeta = 1$) or jamming ($\zeta \simeq$ const. < 1) occurs.

R5: Finally, we proceed from (C6) and keep the shape parameter fixed ($\zeta \simeq$ const.). We let the simulation run for further $\tau_{\mathrm{r}} + \tau_{\mathrm{s}} \sim 10^8$ (and harvest further configurations), where the system relaxes or becomes stationary.

In our results, we mostly report the quantity τ that we define as the total number of Monte Carlo time steps starting subsequent to (C4), i.e., $\tau = \tau_{\mathrm{d}} + \tau_{\mathrm{r}} + \tau_{\mathrm{s}}$. Hence, (C4) represents the reference configuration ($\tau \simeq 0$) for calculating the MSD $r^2(\tau)$. In order to appropriately compare the long-time diffusion after the sweeps with the equilibrium results, we introduce τ' as the total number of Monte Carlo time steps starting from (C6), i.e., $\tau' = \tau_{\mathrm{r}} + \tau_{\mathrm{s}}$. In this case, we consistently consider (C6) as the reference configuration ($\tau' \simeq 0$) for calculating the MSD $r^2(\tau')$.

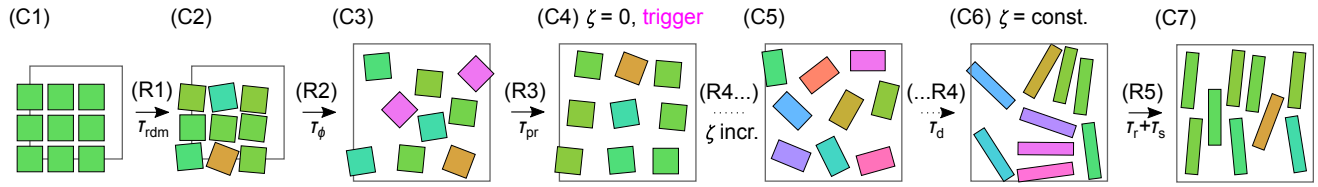

FIG. S1. Schematic of the simulation protocol. The sketches represent snapshots of simplified configurations (Cx) composed of hard particles (color indicates orientation) within a simulation box (gray) for a fixed state. The sequences of simulation runs (Rx) establish the chronological workflow.

---

[1] Since we perform Monte Carlo simulations, we identify a time step $\Delta\tau = 1$ as (approximately) one local (translation or rotation) trial move per particle, i.e., τ represents the order of magnitude of performed local (translation or rotation) trial moves per particle.
[2] Either a local translation or rotation trial move is randomly selected with probability $p_{\mathrm{t}} = 0.5$ for a translation move.
[3] Either a trial move (translation/rotation) or a shape update attempt is randomly selected with probability $p_{\mathrm{s}} = 0.5$ for a shape update attempt.

For the equilibrium results with constant shape, we proceed analog to Fig. S1 except for omitting the shape updates (and pre-relaxation), i.e., the systems are prepared at high packing fractions analog to (C1), and the runs (R3) and (R4) are spared. The relaxation is performed for $\tau_\mathrm{r} \sim 4 \times 10^7$. In the stationary regime, we run for further $\tau_\mathrm{s} \sim 2 \times 10^8$ and periodically collect $\sim 2 \times 10^4$ configurations. Accordingly, we start counting τ' after the relaxation for τ_r is accomplished, i.e., for the equilibrium results $\tau' = \tau_\mathrm{s}$ holds.

Note that all shapes perform rotation and translation trial moves (with probability $p_\mathrm{t} = 0.5$ for a translation move) except for the non-orientable disk. Thus, we weight each MC time step for disks with a factor of 2 in our post-analysis (i.e., $\tau_{\mathrm{disk,\ eff}} = 2\tau_\mathrm{disk}$) in order to achieve an appropriate comparison of the MSDs and diffusion coefficients with the other (orientable) shapes.

All shapes exhibit a constant area of σ^2, resulting in the following order of circumference diameters of the shapes (sorted in ascending order): disk, (regular) pentagon, square, (regular) triangle, and rectangle with aspect ratio $\alpha = 15$. If not explicitly stated otherwise, all systems are composed of $N \sim 10^3$ particles, and for all state points, averages are calculated from $\lesssim 30$ trajectories with different random number seeds.

S2. FINITE-SIZE ANALYSIS OF THE FINAL SHAPE PARAMETER

Finite-size effects on the final shape parameter values ζ_f are investigated in Fig. S2. In the morphing protocol, we observe the reasonable trend that the larger the system size the more simulation runs of the sweep at high packing fraction ($\phi = 0.88$) terminate at $\zeta_\mathrm{f} = 1$. On the contrary, the sharp peaks corresponding to the sweeps at high packing fractions ($\phi = 0.72$, 0.80 and 0.88) of the cascading protocol do not show a dependency on the system size and remain at distinct values of ζ_f.

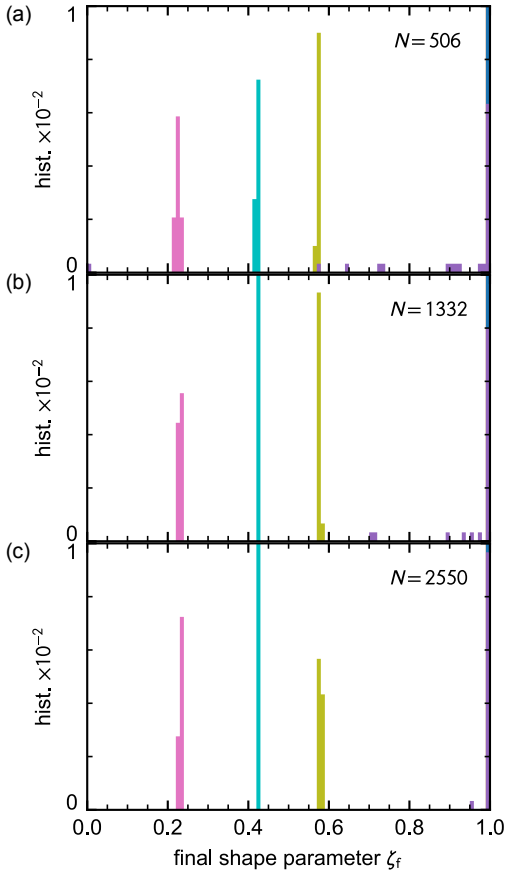

FIG. S2. Distribution of the final shape parameter values ζ_f in our morphing and cascading protocol systems for the five pairs of sweeps with constant $\phi = 0.32$, 0.49, 0.72, 0.80 and 0.88. Three system sizes are compared with different numbers N of particles: (a) $N = 506$, (b) $N = 1332$ and (c) $N = 2550$. In any case, $\langle \zeta_\mathrm{f} \rangle = 1$ is always reached, except: morphing protocol with $\phi = 0.88$ (purple) and cascading protocol with $\phi = 0.72$ (olive), 0.80 (cyan) and 0.88 (pink). For each shape transformation protocol, sweep and system size, we have performed $\lesssim 30$ simulation runs with different random number seeds.

S3. EFFECTIVE DIFFUSION COEFFICIENT

The equilibrium MSDs (particle and MC time step averages) for various shapes at nonvanishing packing fractions ($\phi > 0$) are shown in Fig. S3(a)-(e). For calculating MSDs, we employ the package `freud` [5]. As a reference, long-time fits (not shown) according to the normal diffusion model

$$r^2(\tau) = 2dD_{\text{eff}}\tau \tag{S1}$$

yield the effective diffusion coefficients D_{eff} in Fig. S3(f).

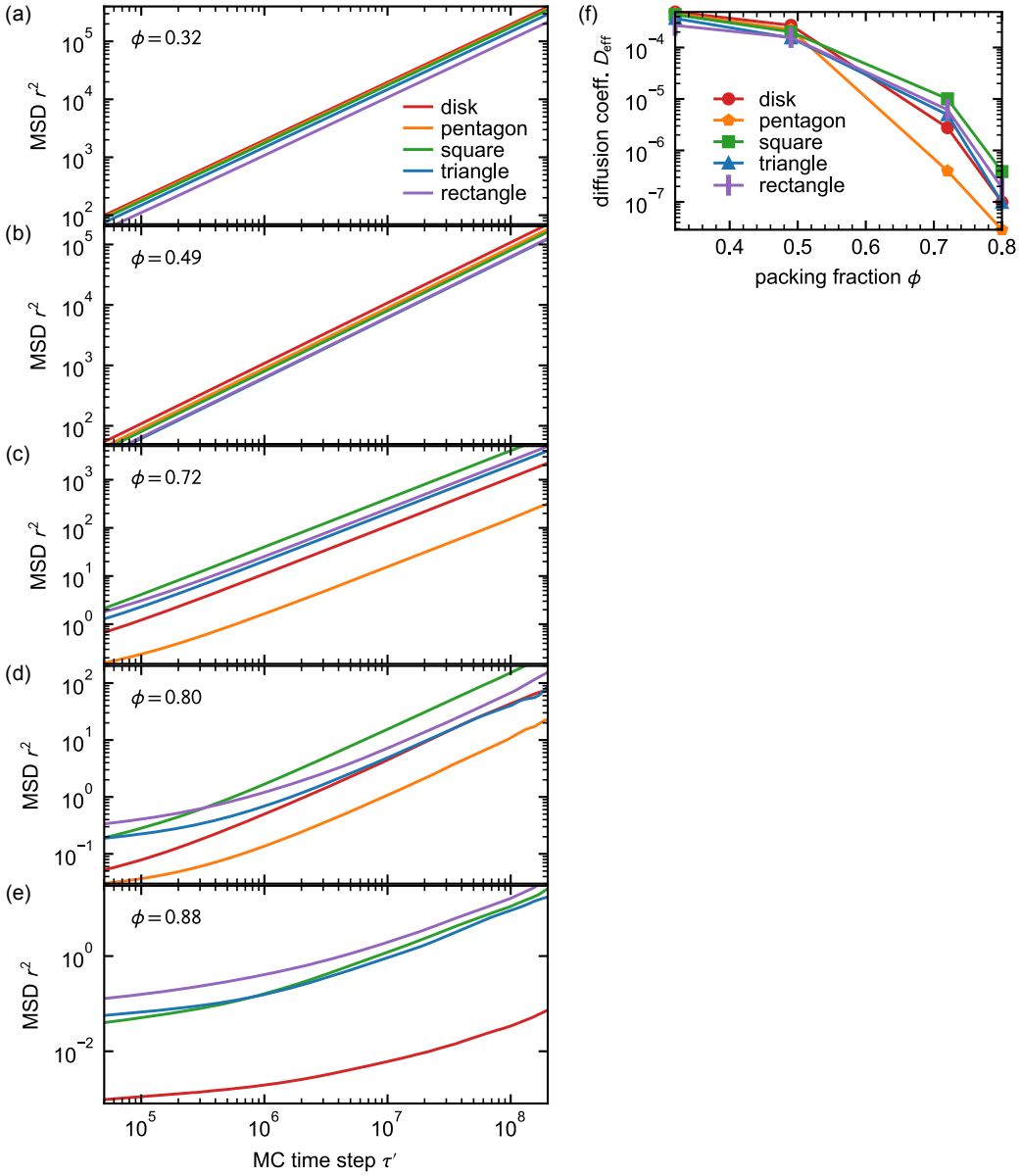

FIG. S3. Equilibrium MSD (particle and MC time step averages) for hard disks (red), (regular) pentagons (orange), squares (green), (regular) triangles (blue) and rectangles with aspect ratio $\alpha = 15$ (purple) at constant packing fractions (a) $\phi = 0.32$, (b) 0.49, (c) 0.72, (d) 0.80, and (e) 0.88. For (regular) pentagons, the further compression to the highest target packing fraction ($\phi = 0.88$) was not reached within finite compression times in the same order of magnitude as for the other shapes. (b) Long-time effective diffusion coefficient D_{eff} for hard disks (red), pentagons (orange), squares (green), triangles (blue), and rectangles with aspect ratio $\alpha = 15$ (purple). D_{eff} has been estimated fitting (not shown) the linear regime in (a)-(e) according to the normal diffusion model.

S4. DIFFUSION COEFFICIENT OF SPHERES, DISKS AND RODS (ANALYTICAL)

Sphere. The diffusion coefficient of a sphere is known from the Einstein relation [6]

$$D_0^{\mathrm{s}} = \frac{k_{\mathrm{B}}T}{b^{\mathrm{s}}} = \frac{k_{\mathrm{B}}T}{6\pi\eta_0\varrho^{\mathrm{s}}} \simeq 3.81\ \mu\mathrm{m}^2/\mathrm{s}. \tag{S2}$$

For the evaluation, we have considered a spherical particle with radius $\varrho^{\mathrm{s}} = \sqrt{\sigma^2/\pi}$ (i.e., same radius as for a disk of area σ^2) with $\sigma = 100$ nm in a solvent of viscosity $\eta_0 = 0.01$ poise at temperature $T = 293.15$ K.
Infinitely thin disk. For an infinitely thin disk, the diffusion coefficient reads [7–11]

$$D_0^{\mathrm{d}} = \frac{k_{\mathrm{B}}T}{6\pi\eta_0\varrho_{\mathrm{h}}^{\mathrm{d}}} \simeq 5.98\ \mu\mathrm{m}^2/\mathrm{s}, \tag{S3}$$

with the hydrodynamic radius $\varrho_{\mathrm{h}}^{\mathrm{d}} = 2\varrho^{\mathrm{d}}/\pi$ in terms of the actual radius $\varrho^{\mathrm{d}} = \sqrt{\sigma^2/\pi}$. We have evaluated this formula for the same conditions as for the sphere.
Long and thin rod. The average translational diffusion coefficient of a long and thin rod with aspect ratio α can be estimated as [6]

$$D_0^{\mathrm{rod}}(\alpha) \simeq \frac{k_{\mathrm{B}}T}{3\pi\eta_0\sqrt{\alpha}\sigma}\ln(\alpha). \tag{S4}$$

Analytical results. The analytical results are compared under the same conditions with the subsequent hydrodynamic calculations results for various shapes in Fig. S4(c). All values lie in the same order of magnitude.

S5. HYDRODYNAMIC (HD) CALCULATION OF THE DIFFUSION COEFFICIENTS OF ARBITRARY SHAPES

Introduction. Hydrodynamic properties of particles can be computed by employing a bead model [7, 12], where the shape is represented by a rigid set of spherical particles. For our morphing and cascading protocol, we present in Fig. S4(a) and (b) examples of the masks for the bead models. Given the positions $\{\mathbf{r}_i\}_{i=1}^{N^{\mathrm{b}}}$ and radii $\{\varrho_i^{\mathrm{b}}\}_{i=1}^{N^{\mathrm{b}}}$ of the beads, the hydrodynamic interactions are described for each pair (i,j) by a $d\times d$ symmetric tensor [7, 13]. Hereinafter, the formal procedure would begin with the construction of the $dN^{\mathrm{b}} \times dN^{\mathrm{b}}$ diffusion supermatrix $\mathcal{S}$ and result in the generalized friction matrix $\mathbf{B}$ [7, 12]. Then, the generalized diffusion matrix $\mathbf{D}$ follows from the generalized Einstein equation [12, 14]

$$\mathbf{D} = k_{\mathrm{B}}T\mathbf{B}^{-1} \tag{S5}$$

that governs the Brownian and frictional behavior of a rigid particle. Here, the generalized matrices for diffusion and friction,

$$\mathbf{D} = \begin{pmatrix} \mathbf{D}^{\mathrm{tt}} & \mathbf{D}^{\mathrm{rt}} \\ \mathbf{D}^{\mathrm{tr}} & \mathbf{D}^{\mathrm{rr}} \end{pmatrix} \quad \text{and} \quad \mathbf{B} = \begin{pmatrix} \mathbf{B}^{\mathrm{tt}} & \mathbf{B}^{\mathrm{rt}} \\ \mathbf{B}^{\mathrm{tr}} & \mathbf{B}^{\mathrm{rr}} \end{pmatrix}, \tag{S6}$$

respectively, have each the form of a $2d \times 2d$ matrix that is composed of four $d \times d$ blocks: $\mathbf{X}^{\mathrm{tt}}$ for translation, $\mathbf{X}^{\mathrm{rr}}$ for rotation, $\mathbf{X}^{\mathrm{tr}}$ for translation-rotation coupling, and $\mathbf{X}^{\mathrm{rt}} = (\mathbf{X}^{\mathrm{tr}})^{\top}$ with $\mathbf{X} \in \{\mathbf{D}, \mathbf{B}\}$. Finally, the (orientation-averaged) translational diffusion coefficient of a free particle is obtained from [6, 7, 15]

$$D_0^{(\mathrm{HD})} = \frac{1}{d}\,\mathrm{tr}\left(\mathbf{D}^{\mathrm{tt}}\right). \tag{S7}$$

The treatment of nanoplatelets with a specified thickness h can be carried out analog to the bead modeling with spherical elements in three dimensions and is explained in Ref. [7].
Calculation details. Our geometric raw input masks of the planar structures that are described as a superposition of circles are processed and prepared as the corresponding bead models by the program `HYDRO2D-Circles` [7] for the subsequent calculation of the hydrodynamic coefficients and other solution properties, where we employ the program `HYDRO++` [12, 16–18]. For the hydrodynamic calculations[4], we assume a temperature of $T = 20.0$ °C, a

[4] Additionally, we have set in the program as an approximation a particle density of $\rho_{\mathrm{particle}} = 1.7$ g/cm^3 [19, 20] and a solvent density of $\rho_{\mathrm{solvent}} = 1.0$ g/cm^3, which are mainly relevant for other solution properties.

solvent viscosity of $\eta = 0.01$ poise, a hexagonal non-overlapping lattice arrangement, and consider two hydrodynamic thickness values ranging from $h_{\min} = 2.99$ nm to $h_{\max} = 3.01$ nm. The latter choice is used as approximation for DNA duplexes, based on the bare double helix diameter of 2.0 nm and an additional hydration layer of approximately 0.3 nm [21]. The results are summarized in Fig. S4(c).

S6. BROWNIAN DYNAMICS (BD)

Free diffusion. In the special case of free diffusion, the Brownian dynamics are purely stochastic and the MSD obeys the normal diffusion model [6, 15]

$$r^2(t) = 2dD_0^{(\mathrm{BD})}\, t, \tag{S8}$$

so that a linear fit to the MSD yields the single-particle (isotropic) translational diffusion coefficient $D_0^{(\mathrm{BD})}$. Note that the previous `HYDRO++` calculation of the translational diffusion coefficient $D_0^{(\mathrm{HD})}$ in Eq. (S7) of an isolated particle corresponds to this $D_0^{(\mathrm{BD})}$, as it assumes a single particle in a continuum solvent (limit of infinite dilute solution) [7, 12, 16], i.e., $D_0 = D_0^{(\mathrm{HD})} \simeq D_0^{(\mathrm{BD})}$. This is also clear by construction due to consistency of the trace calculation in Eq. (S7) and the fluctuation-dissipation relation underlying the Brownian dynamics [6, 15].
Brownian time. The characteristic Brownian time

$$t_{\mathrm{B}} = \frac{\sigma^2}{2dD_0}, \tag{S9}$$

is defined as the time for a particle to diffuse a distance $\sim \sigma$ comparable to its own size $\sim \sigma$. According to our theoretical prediction, a typical DNA origami nanostructure (under standard laboratory conditions) with a characteristic length scale of $\sigma = 100$ nm [22], exhibits a Brownian time $t_{\mathrm{B}} \sim 10^{-1}$ ms [cf. Fig. S4(d)]. Note that this timescale is several orders of magnitudes smaller than the duration $\Delta t_{\mathrm{origami}} \sim 10$ min of the experimental DNA origami shape transformation process [22]. This motivates our quasi-static shape transformation approach with very small shape changes. In the present study, we use for time normalization the Brownian time $t_{\mathrm{B}} \simeq 0.289$ ms of our thin (thickness $h \simeq 3$ nm) disk of radius $\varrho^{\mathrm{d}} = \sqrt{\sigma^2/\pi}$.

S7. TRANSLATIONAL DIFFUSION COEFFICIENTS AND CHARACTERISTIC BROWNIAN TIMES FOR VARIOUS SHAPES

The translational diffusion coefficients and characteristic Brownian times for various shapes are summarized in Fig. S4(c) and (d), respectively. The apparent small plateaus and locally non-monotonic behavior in the numerical hydrodynamic calculation results of D_0 in Fig. S4(c) can be attributed to the limited resolution (discretization) and small effective particle size changes in the underlying mask for the bead model approximation of the shapes [cf. Fig. S4(a) and (b)].

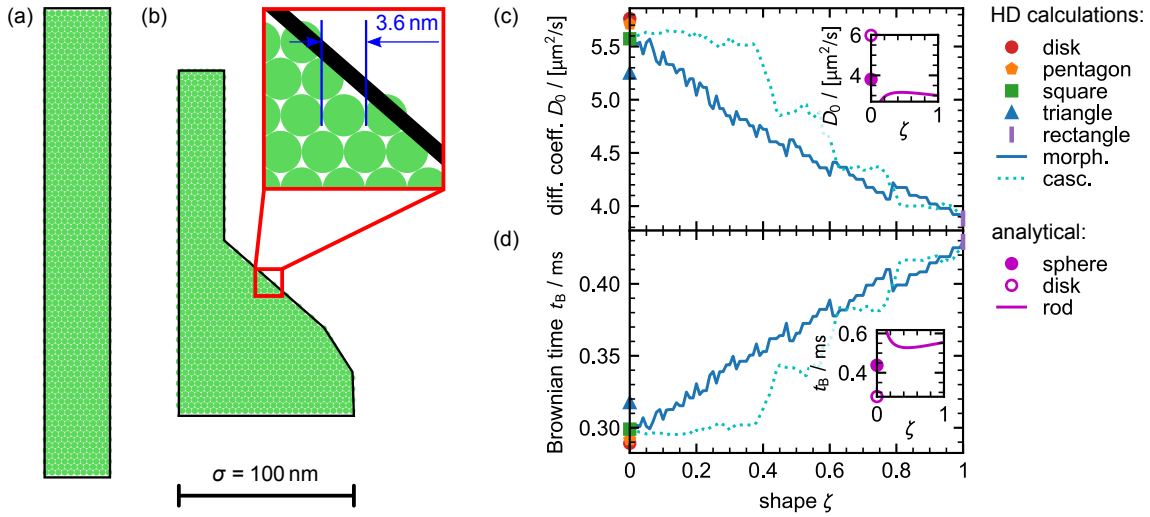

FIG. S4. Mask for the bead model, hydrodynamic (HD) calculations, and analytical results for various shapes. (a/b) Geometric raw input mask of the planar structure that is approximated as a superposition of circles (represented by the green disks) for the subsequent construction of the bead model of a morphing/cascading protocol shape for the exemplary shape parameter $\zeta = 0.44$. The black polygon shows the shape used in the MC simulations, where all shapes exhibit a constant area of σ^2 (e.g., $\sigma^2 = 0.01\ \mu\text{m}^2$ for the length scale $\sigma = 100$ nm [22]). The inset displays a zoom into a small region in the neighborhood of the boundary. In total, we use a number $\simeq 900$ of raw input mask circles with a diameter of 3.6 nm. (c) and (d) (Avg.) translational (free) diffusion coefficient D_0 and Brownian time t_B for the morphing (solid blue) and cascading (dotted cyan) protocol as a function of the shape parameter ζ, respectively. At $\zeta = 0$, we also show the HD calculation values for a disk (red closed disk), pentagon (orange closed pentagon), square (green closed square), and triangle (blue closed triangle). Additionally, the HD calculation value of the rectangle of aspect ratio $\alpha = 15$ (purple closed rectangle) is shown at $\zeta = 1$, where the morphing and cascading protocol finish. The insets show the evaluation of analytical calculations for a spherical particle (magenta closed disk) in Eq. (S2), for an infinitely thin disk in Eq. (S3) (magenta open disk), and for a long and thin rod (magenta solid curve) in Eq. (S4), where the aspect ratio α of the latter is bijectively mapped to the shape parameter ζ as $\zeta = (\alpha - 1)/14$. Note that for too small values of ζ, the underlying assumption of a long rod can be violated. The underlying parameters correspond to typical DNA origami nanostructures under standard laboratory conditions specified in the text.

S8. CALIBRATION AND REDUCED QUANTITIES (BROWNIAN TIME RESCALING)

For each shape, we calculate the conversion factor

$$c(\zeta) = \frac{D_{\mathrm{eff},0}}{D_0(\zeta)}, \tag{S10}$$

where D_0 is known from our previous HD calculations. The effective free diffusion coefficient $D_{\mathrm{eff},0}$ is analytically deduced from the HPMC algorithm, where the MSD in the dilute limit follows as

$$r^2 = \int_{|\mathbf{r}|\leq\urcorner} \mathrm{d}^d\mathbf{r}\; r^2\, \mathcal{P}(\mathbf{r}) = \frac{S_{d-1}}{V_d(\urcorner)} \int_0^{\urcorner} \mathrm{d}r\; r^{d+1} = \frac{d}{d+2}\urcorner^2 \tag{S11}$$

with the probability density $\mathcal{P}$ for uniform sampling inside a d-dimensional ball of radius $\urcorner$. We use this result to determine the effective diffusion coefficient in Eq. (S1) per (effective translational) MC time step (formally: $\Delta\tau_{\mathrm{t,eff}} \mathrel{\widehat{=}} (p_{\mathrm{t}}P_{\mathrm{t}}^{\mathrm{acc}})^{-1}$) as

$$D_{\mathrm{eff},0} = \frac{r^2}{2d(p_{\mathrm{t}}P_{\mathrm{t}}^{\mathrm{acc}})^{-1}} = \frac{p_{\mathrm{t}}P_{\mathrm{t}}^{\mathrm{acc}}}{2(d+2)}\urcorner^2 = 1.225\times10^{-3}\sigma^2, \tag{S12}$$

where we have used for the evaluation the translation move probability $p_{\mathrm{t}} = 0.5$, maximum size $\urcorner = 0.14\sigma$ of displacement trial moves, dimensionality $d = 2$, and approximately assume $P_{\mathrm{t}}^{\mathrm{acc}} \simeq 1$.

Accordingly, the conversion factor c maps one MC time step to an equivalent amount of physical (Brownian) time by matching the free-particle diffusion rates in hard-particle MC and BD simulation (the latter coincidence with hydrodynamic calculations). The conversion factors c for all shapes and protocols are summarized in Fig. S5.

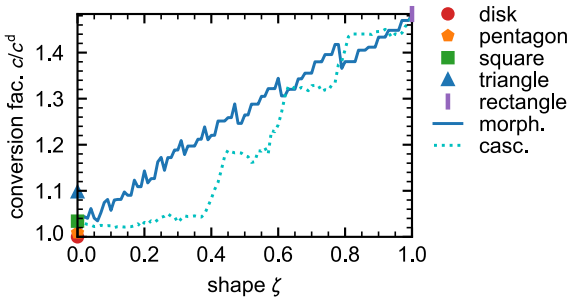

FIG. S5. Conversion factors c between MC time step and physical (Brownian) time for all shapes and protocols [cf. Eq. (S10)]. The data points correspond to our hard disk (red), pentagon (orange), square (green), triangle (blue), and rectangle with aspect ratio $\alpha = 15$ (purple). Also shown are the curves for the morphing (solid blue) and cascading (dotted cyan) protocol. For normalization, we use the value $c^{\mathrm{d}} = 7.35\times10^{-3}\times[t_{\mathrm{B}}/\mathrm{MC\ step}] \simeq 2.13\ \mu\mathrm{s/MC\ step}$ of our thin disk.

The conversion factors c enable an approximate determination of the actual diffusion coefficient and time for each shape as

$$D \sim \frac{D_{\mathrm{eff}}}{c}, \quad \mathrm{d}t \sim c\,(\zeta(\tau))\;\mathrm{d}\tau. \tag{S13}$$

Here, the MC time step integration is numerically approximated via the cumulative trapezoidal rule. In our main text, we employ reduced quantities, i.e., we report the reduced diffusion coefficient D/D_0 and the reduced time t/t_{B} (with $t_{\mathrm{B}} \simeq 0.289$ ms of our thin (thickness $h \simeq 3$ nm) disk of radius $\varrho^{\mathrm{d}} = \sqrt{\sigma^2/\pi}$).

S9. COMPARISON OF THE MORPHING AND CASCADING PROTOCOL

At higher packing fractions, the cascading protocol does not recover from the slow-down and the dynamics is arrested, resulting in a flattening of shape and MSD curves reaching a constant value (cf. main text). To get some insight into the origin of the dynamic arrest, in Fig. S6 we show a sequence of snapshots for both protocols. At this packing fraction ($\phi = 0.49$), a completion of the shape transformation is achieved for both protocols. However, the cascading protocol already shows a temporal slow-down of the dynamics in the neighborhood of Fig. S6(e). The reason is the temporal high value of the effective packing fraction $\phi_{\text{eff}} \simeq 0.9$ occurring during the cascading sweep (cf. main text).

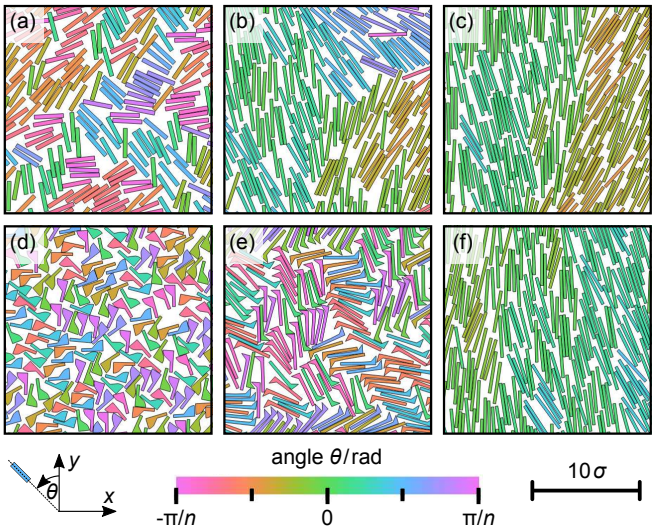

FIG. S6. Sequences of simulation snapshots (excerpts of the full system) for sweeps at packing fraction $\phi = 0.49$ comparing the morphing (first row) and cascading protocol (second row): (a),(d) intermediate regime (morphing: $t/t_{\text{B}} \simeq 3.9 \times 10^3$, $\zeta \simeq 0.45$; cascading: $t/t_{\text{B}} \simeq 3.8 \times 10^3$, $\zeta \simeq 0.45$), (b),(e) late regime (morphing: $t/t_{\text{B}} \simeq 7.5 \times 10^3$, $\zeta \simeq 0.83$; cascading: $t/t_{\text{B}} \simeq 7.7 \times 10^3$, $\zeta \simeq 0.81$), and (c),(f) stationary regime (morphing: $t/t_{\text{B}} \simeq 1.7 \times 10^4$, $\zeta = 1.00$; cascading: $t/t_{\text{B}} \simeq 1.7 \times 10^4$, $\zeta \simeq 1.00$). The particle color takes the n-fold symmetry of the shape into account (with $n = 2$ for rectangles and $n = 1$ else).

S10. SYSTEM SIZE DEPENDENCE OF THE SHAPE, DIFFUSION AND ORDER PROPERTIES

The effect of different system sizes on the evolution of the shape parameter, MSD and orientational order is analyzed in Fig. S7. Mostly, we find close accordance, except for slight deviations for the smallest system size occurring in the morphing protocol sweeps at high packing fractions ($\phi > \phi_c \simeq 0.54$). This effect primarily addresses the corresponding quantitative manifestation of orientational order during the dynamics [e.g., cf. Fig. S7(Mo) and (Mt)].

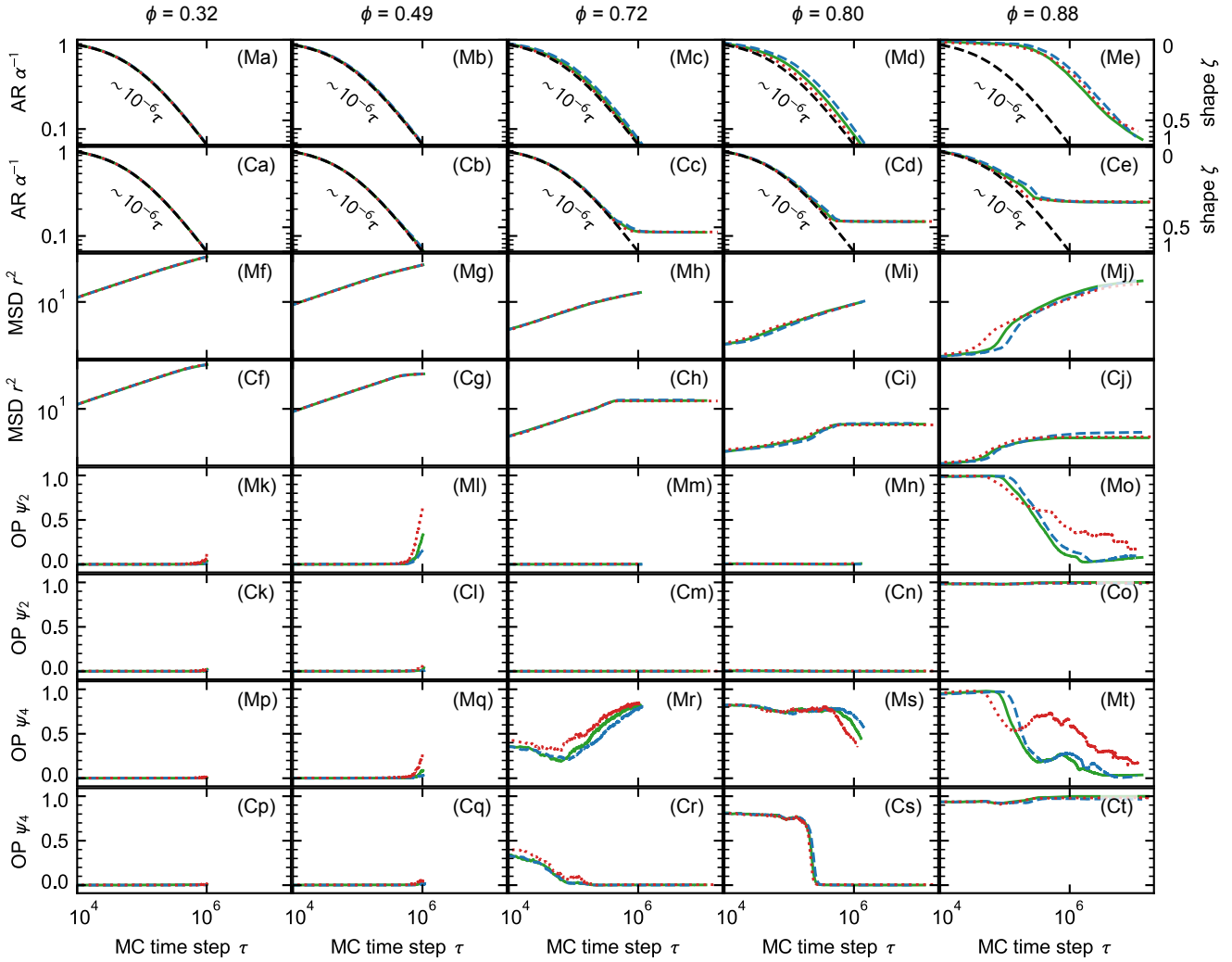

FIG. S7. Finite-size effects in our morphing (Mx) and cascading (Cx) protocol systems for the five pairs of sweeps with constant $\phi = 0.32$ (first column), 0.49 (second column), 0.72 (third column), 0.80 (fourth column) and 0.88 (fifth column). We investigate the (Xa-e) evolution of the shape parameter ζ, (Xf-j) MSD (only particle averages), and (Xk-t) orientational order $\psi_{2/4}$ (cf. main text). Three system sizes are compared with different numbers N of particles: $N = 506$ (dotted red), $N = 1332$ (solid green) and $N = 2550$ (dashed blue). For each system size, the average calculation is based on $\lesssim 30$ simulation runs with different random number seeds.

S11. EQUILIBRIUM ORDER PROPERTIES IN HARD RECTANGLE SYSTEMS

Fig. S8 summarizes the equilibrium properties of the family of hard rectangles with aspect ratio $\alpha \in (1, 15]$ ($\Leftrightarrow \zeta \in (0, 1]$).

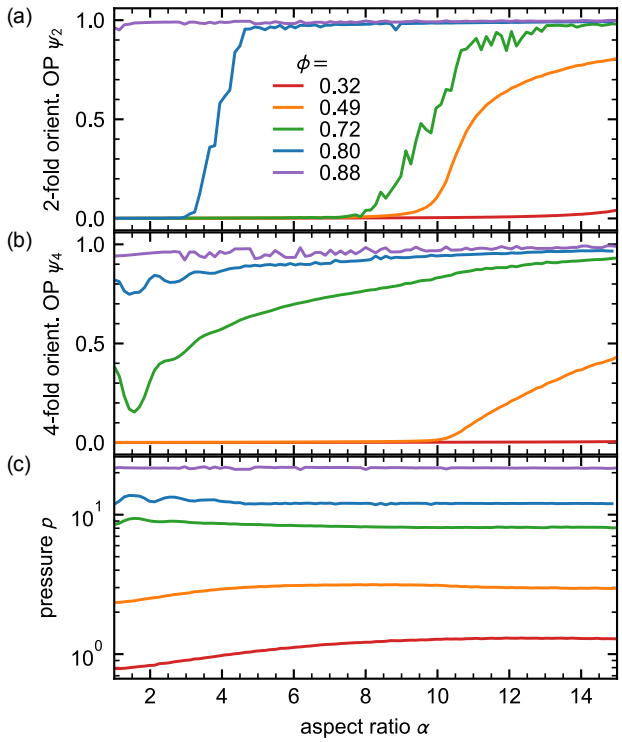

FIG. S8. Equilibrium properties of hard rectangles with aspect ratio α at constant packing fractions $\phi = 0.32$ (red), 0.49 (orange), 0.72 (green), 0.80 (blue), and 0.88 (purple). (a) and (b) 2- and 4-fold orientational order parameter $\psi_{2/4}$, respectively. (c) Eq. of state. For each state point (α, ϕ), the averages of the observables are calculated from a single trajectory with individual random number seeds. We recapitulate that the systems have been prepared in the smectic phase and follow the expansion path.

[1] J. A. Anderson, C. D. Lorenz, and A. Travesset, General purpose molecular dynamics simulations fully implemented on graphics processing units, J. Comput. Phys. **227**, 5342 (2008).

[2] J. Glaser, T. D. Nguyen, J. A. Anderson, P. Lui, F. Spiga, J. A. Millan, D. C. Morse, and S. C. Glotzer, Strong scaling of general-purpose molecular dynamics simulations on GPUs, Comput. Phys. Commun. **192**, 97 (2015).

[3] J. A. Anderson, M. Eric Irrgang, and S. C. Glotzer, Scalable Metropolis Monte Carlo for simulation of hard shapes, Comput. Phys. Commun. **204**, 21 (2016).

[4] J. A. Anderson, J. Glaser, and S. C. Glotzer, HOOMD-blue: A Python package for high-performance molecular dynamics and hard particle Monte Carlo simulations, Comput. Mater. Sci. **173**, 109363 (2020).

[5] V. Ramasubramani, B. D. Dice, E. S. Harper, M. P. Spellings, J. A. Anderson, and S. C. Glotzer, Freud: A software suite for high throughput analysis of particle simulation data, Comput. Phys. Commun. **254**, 107275 (2020).

[6] J. K. G. Dhont, *An Introduction to Dynamics of Colloids*, Studies in Interface Science No. 2 (Elsevier, Amsterdam, Netherlands, 1996).

[7] J. G. Hernández-Cifre, R. Rodríguez-Schmidt, C. M. Almagro-Gómez, and J. García De La Torre, Calculation of the friction, diffusion and sedimentation coefficients of nanoplatelets of arbitrary shape, Polymer **262**, 125467 (2022).

[8] A. Oberbeck, Ueber stationäre Flüssigkeitsbewegungen mit Berücksichtigung der inneren Reibung., Journal für die reine und angewandte Mathematik (Crelles Journal) **1876**, 62 (1876).

[9] H. Lamb, *Hydrodynamics*, unabridged and unaltered republ. of the 6. ed., cambridge 1932 ed. (Dover Publ, New York, 2005).

[10] G. K. Batchelor, *An Introduction to Fluid Dynamics*, 14th ed., Cambridge Mathematical Library (Cambridge Univ. Press, Cambridge, 2010).

[11] J. Happel and H. Brenner, *Low Reynolds Number Hydrodynamics: With Special Applications to Particulate Media*, 2nd ed., Mechanics of Fluids and Transport Processes (Kluwer Acad. Publ, Dordrecht, 1991).
[12] J. García De La Torre, G. Del Rio Echenique, and A. Ortega, Improved Calculation of Rotational Diffusion and Intrinsic Viscosity of Bead Models for Macromolecules and Nanoparticles, J. Phys. Chem. B **111**, 955 (2007).
[13] J. G. De La Torre and V. A. Bloomfield, Hydrodynamic properties of macromolecular complexes. I. Translation, Biopolymers **16**, 1747 (1977).
[14] H. Brenner, Coupling between the translational and rotational brownian motions of rigid particles of arbitrary shape, Journal of Colloid and Interface Science **23**, 407 (1967).
[15] M. X. Fernandes and J. G. De La Torre, Brownian Dynamics Simulation of Rigid Particles of Arbitrary Shape in External Fields, Biophysical Journal **83**, 3039 (2002).
[16] J. Garcia De La Torre, S. Navarro, M. Lopez Martinez, F. Diaz, and J. Lopez Cascales, HYDRO: A computer program for the prediction of hydrodynamic properties of macromolecules, Biophysical Journal **67**, 530 (1994).
[17] J. G. De La Torre and V. A. Bloomfield, Hydrodynamic properties of complex, rigid, biological macromolecules: Theory and applications, Quart. Rev. Biophys. **14**, 81 (1981).
[18] B. Carrasco and J. García De La Torre, Hydrodynamic Properties of Rigid Particles: Comparison of Different Modeling and Computational Procedures, Biophysical Journal **76**, 3044 (1999).
[19] F. Amalric and J. Zalta, Rat hepatoma cells nucleolar DNA. I. Analysis of nucleolar DNA, Nucl Acids Res **2**, 1305 (1975).
[20] Y. Yang, Z. Wu, L. Wang, K. Zhou, K. Xia, Q. Xiong, L. Liu, Z. Zhang, E. R. Chapman, Y. Xiong, T. J. Melia, E. Karatekin, H. Gu, and C. Lin, Sorting sub-150-nm liposomes of distinct sizes by DNA-brick-assisted centrifugation, Nat. Chem. **13**, 335 (2021).
[21] J. García De La Torre and J. G. Hernández-Cifre, Hydrodynamic properties of macromolecules and nanoparticles in dilute solution: A brief essay on classical and modern concepts, Eur Biophys J **54**, 331 (2025).
[22] D. Wang, L. Yu, B. Ji, S. Chang, J. Song, and Y. Ke, Programming the Curvatures in Reconfigurable DNA Domino Origami by Using Asymmetric Units, Nano Lett. **20**, 8236 (2020).